Applied Mathematical Modelling 151 (2026) 116491

Contents lists available at ScienceDirect

Applied Mathematical Modelling

journal homepage: www.elsevier.com/locate/apm

Analytical solution for dynamic response of multi-span bridges under moving loads: an efficient method based on time-discrete analysis using sinc interpolation

A. Romero [a,*], E. Moliner [b], M. D. Martínez-Rodrigo [b], P. Galvín [a,c]

[a] Escuela Técnica Superior de Ingeniería, Universidad de Sevilla, Camino de los Descubrimientos s/n, ES-41092, Sevilla, Spain
[b] Department of Mechanical Engineering and Construction, Universitat Jaume I, Avda. Sos Baynat s/n, ES-12071, Castellón, Spain
[c] Laboratory of Engineering for Energy and Environmental Sustainability, ENGREEN, Universidad de Sevilla, Camino de los Descubrimientos s/n, ES-41092, Sevilla, Spain

ARTICLE INFO

Keywords:
Railway bridges
Moving loads
Railway traffic
Analytical solution
Time-discrete analysis
Sinc interpolation
Open-source code

ABSTRACT

This paper proposes an analytical method for calculating the dynamic response of multi-span bridges subjected to moving loads. The proposed approach uses sinc interpolation time-discrete analysis based on the Nyquist-Shannon sampling theorem. The proposed method enables the computation of dynamic responses with analytical precision and minimal computational effort. This work provides closed-form explicit formulas for bridge response with significant advantages over conventional numerical approaches, reducing complexity and computational cost without compromising accuracy. Validation cases demonstrated the robustness and reliability of the proposed solution for different bridge configurations and loading scenarios. To facilitate adoption, the proposed methodology is implemented in open-source Julia code, which is available at GitHub. In addition to providing a powerful toolbox for structural engineers, this study establishes a foundational framework for extending sinc-based interpolation techniques to other structural dynamics and civil engineering problems.

1. Introduction

The development of a Single European Railway Area (SERA) is a key objective of the Europe's Rail Joint Undertaking (EU-Rail) [1], aiming to harmonise standards and improve interoperability across Europe. A critical challenge in this initiative is to enhance the structural analysis of railway bridges to optimise capacity, service quality and cost efficiency. Railway bridges play a fundamental role in rail transport networks, yet their dynamic response to moving loads remains a complex issue requiring advanced methodologies for accurate assessment.

The InBridge4EU project [2], launched under Horizon Europe research and innovation programme, seeks to develop a dynamic interface between railway bridges and rolling stock. The project introduces new methodologies aligned with existing European regulations, INF TSI [3], LOC&PAS TSI [4], EN 15,528 [5], EN 1990-Annex A2 [6], and EN 1991-2 [7]. A key focus of the project is the assessment of the existing railway bridge infrastructure through a comprehensive dataset covering over 500 bridges from 10 railway lines across five EU countries. This analysis requires transient dynamic Time Step Calculation (TSC) simulations, integrating real

* Corresponding author.
E-mail address: aro@us.es (A. Romero).

https://doi.org/10.1016/j.apm.2025.116491
Received 6 May 2025; Received in revised form 25 September 2025; Accepted 3 October 2025
Available online 13 October 2025
0307-904X/

train models and newly defined Dynamic Train Categories (DTCs). Given the scale of this research, efficient and accurate numerical methods are required to ensure robust and fast evaluations.

The dynamic response of multi-span beams such as railway bridges is significantly influenced by moving loads, necessitating sophisticated analytical and computational techniques for their precise assessment [8,9]. Various methodologies, including analytical approaches, numerical modelling, and experimental testing, have been developed to address the dynamic behaviour of beams and bridges subjected to moving loads. However, limitations such as numerical instabilities, computational inefficiencies, and discrepancies in long-duration simulations remain key challenges. The need for more reliable and computationally efficient methods to enhance railway bridge safety and longevity is therefore of interest.

Despite advancements in numerical and analytical techniques, existing methods for modelling moving load problems often suffer from algorithmic instabilities or excessive computational demands. The Laplace transform has shown promise in solving time-domain structural dynamics problems; however, there are limitations due to numerical inaccuracies. Alternative approaches, such as numerical Laplace inversion techniques and finite element formulations based on Hamilton's variational principle, have been proposed to mitigate these issues [10,11].

Martínez-Castro et al. [12] and García-Macías and Martínez-Castro [13] developed a semi-analytical solution and a model based on the Hilbert transform to evaluate the response of non-uniform multi-span beams subjected to moving loads. These approaches allowed fast computation with minimal loss of accuracy. Johansson et al. [14] proposed a closed-form solution for the analysis of multi-span beams by applying the Laplace transform to mode superposition governing equations, allowing the calculation of the normal coordinate in the frequency domain. Multi-span beam bridges were modelled by assembling several mode shape functions. However, there remains a need for accurate methodologies, that ensure computational efficiency and stability in transient dynamic analyses.

This paper proposes an analytical method for computing the dynamic response of multi-span railway beams with general boundary conditions subjected to moving loads based on time-discrete analysis using sinc interpolation. The proposed method applies modal superposition by transforming the convolution integrals of normal coordinates into time integrals of trigonometric functions. The main novelty of this work lies in the derivation of closed-form explicit formulas and the application of sinc interpolation. Sinc interpolation allows the reconstruction of continuous band-limited normal coordinates from discrete data points [15–17], ensuring analytical accuracy while minimising computational complexity. This study evaluates different quadrature rules to demonstrate the computational advantages of the proposed approach.

The methodology is implemented in the `SINC-Dyn` function package developed in Julia, which is available on GitHub under the MIT license https://github.com/antonioaro/SincBridgeDynamics.jl, ensuring open access and reproducibility of results.

2. Formulation

2.1. Governing equation of Bernoulli-Euler beam under moving loads

The equation of motion for a Bernoulli-Euler beam of length L subjected to a moving load $p(x,t)$ with velocity V, is given by Frýba [18]:

$$EI\frac{\partial^4 u(x,t)}{\partial x^4} + \mu\frac{\partial^2 u(x,t)}{\partial t^2} = p(x,t), \tag{1}$$

where E denotes Young's modulus, I represents the cross-section moment of inertia, and μ is the mass per unit length. The external force is characterised by its amplitude P_0, Dirac delta function $\delta(t)$, and Heaviside step function $U(t)$:

$$p(x,t) = P_0\delta(x - Vt)\left[U(t) - U\left(t - \frac{L}{V}\right)\right]. \tag{2}$$

The homogeneous solution is assumed to be of the form $u(x,t) = \psi(x)Y(t)$, where $\psi(x)$ represents a spatial function modulated by a time-dependent amplitude $Y(t)$. Substituting this into the equation of motion yields an ordinary differential equation with general solution given by:

$$\psi(x) = \alpha_1 \sin\left(\frac{\lambda}{L}x\right) + \alpha_2 \cos\left(\frac{\lambda}{L}x\right) + \alpha_3 \sinh\left(\frac{\lambda}{L}x\right) + \alpha_4 \cosh\left(\frac{\lambda}{L}x\right), \tag{3}$$

where

$$\lambda^4 = \frac{\mu L^4}{EI}\omega^2, \tag{4}$$

and ω is the angular frequency. The integration constants α_1, α_2, α_3, and α_4 are determined by the boundary conditions related to the displacement, slope, bending moment, and shear force. Consequently, Eq. (3) defines a nonlinear eigenvalue problem, with solutions given by eigenpairs (λ_n, v_n), with $v_n = \{\alpha_{n1}, \alpha_{n2}, \alpha_{n3}, \alpha_{n4}\}$. The mode shapes ψ_n and natural frequencies ω_n of the beam are then given by:

$$\psi_n(x) = \alpha_{n1} \sin\left(\frac{\lambda_n}{L}x\right) + \alpha_{n2} \cos\left(\frac{\lambda_n}{L}x\right) + \alpha_{n3} \sinh\left(\frac{\lambda_n}{L}x\right) + \alpha_{n4} \cosh\left(\frac{\lambda_n}{L}x\right), \tag{5}$$

$$\omega_n = \lambda_n^2\sqrt{\frac{EI}{\mu L^4}}. \tag{6}$$

Assuming linear behaviour, the solution to Eq. (1) can be obtained by mode-superposition analysis defining the displacement in terms of the normal coordinates Y_n as:

$$u(x,t) = \sum_{n=1}^{\infty} \psi_n(x) Y_n(t). \tag{7}$$

Substituting Eq. (7) into Eq. (1) yields:

$$\sum_{n=1}^{\infty} \mu \psi_n(x) \ddot{Y}_n(t) + \sum_{n=1}^{\infty} EI \frac{d^4 \psi_n(x)}{dx^4} Y_n(t) = p(x,t). \tag{8}$$

Multiplying Eq. (8) by ψ_i ($i = 1, 2, \dots$) and integrating over the beam length gives a set of uncoupled equations due to the orthogonality of the mode shapes:

$$M_n \ddot{Y}_n + K_n Y_n = P_n, \quad n = 1, 2, \dots \tag{9}$$

where the modal mass, stiffness, and forcing terms are given by:

$$M_n = \int_0^L |\psi_n^2(x)| \mu \, dx, \qquad K_n = \omega_n^2 M_n, \qquad P_n = \int_0^L \psi_n(x) p(x,t) \, dx. \tag{10}$$

The equation of motion for a damped system can be formulated by introducing the modal damping coefficient $C_n = 2\zeta_n M_n \omega_n$, where ζ_n is the damping ratio:

$$M_n \ddot{Y}_n + C_n \dot{Y}_n + K_n Y_n = P_n, \quad n = 1, 2, \dots \tag{11}$$

or, equivalently:

$$\ddot{Y}_n + 2\zeta_n \omega_n \dot{Y}_n + \omega_n^2 Y_n = \frac{P_n}{M_n}, \quad n = 1, 2, \dots. \tag{12}$$

The following subsections present an analytical solution for the response of a multi-span beam under moving loads.

2.2. *Eigenvalue problem of non-uniform multi-span beams*

The dynamic behaviour of a multi-span beam is described by a piecewise function, as that given in Eq. (5). The beam is modelled as a system of N_e elements of length L_e with local coordinates $x_e \in [0, L_e]$. Each element represents the mode shape ψ_n^e of a particular part of the beam defined by eigenpairs $(\lambda_n^e, \upsilon_n^e)$ according to the boundary conditions, material and cross-section properties. The element representation does not involve discretisation or approximation as in numerical methods. The global coordinate of a point x_e within an element is given by $x = X_{e-1} + x_e$, where X_{e-1} is the starting point in global coordinates:

$$X_{e-1} = \sum_{i=1}^{e-1} L_i, \quad \text{with } X_0 = 0, \tag{13}$$

and the element interval in global coordinates is $\mathcal{L}_e = [X_{e-1}, X_e]$.

The mode shapes and natural frequencies of a multi-span beam are obtained by imposing continuity conditions for displacement, slope, bending moment, and shear force at the joint between elements, as well as support conditions. Then, the mode shapes are given by the piecewise function:

$$\psi_n(x) = \sum_{e=1}^{N_e} \psi_n^e(x) \mathbb{1}_{\mathcal{L}_e}(x) \tag{14}$$

where $\mathbb{1}_{\mathcal{L}_e}(x)$ is the indicator function:

$$\mathbb{1}_{\mathcal{L}_e}(x) = \begin{cases} 1 & \text{if } x \in \mathcal{L}_e \\ 0 & \text{if } x \notin \mathcal{L}_e \end{cases} \tag{15}$$

The element properties and length can be different; thus, an eigenvalue λ_n^e is defined for each element. However, the natural frequency is the same for all elements. Then, the element eigenvalues are related by the dynamic stiffness $\widetilde{K}_e = (EI/\mu L^4)_e$ according to Eq. (6). The element dynamic stiffness is normalised to the element with the minimum stiffness $\widetilde{K}_o = \min_{e=1}^{N_e} \{\widetilde{K}_e\}$, which leads to the definition of $\Lambda_e^4 = \widetilde{K}_o / \widetilde{K}_e$.

Thus, the element eigenvalue is $\lambda_n^e = \Lambda_e \lambda_n$, where λ_n is the eigenvalue of the element with the minimum stiffness. The mode shape of an element becomes:

$$\psi_n^e(x_e) = \alpha_{n1}^e \sin\left(\frac{\Lambda_e \lambda_n}{L_e} x_e\right) + \alpha_{n2}^e \cos\left(\frac{\Lambda_e \lambda_n}{L_e} x_e\right) + \alpha_{n3}^e \sinh\left(\frac{\Lambda_e \lambda_n}{L_e} x_e\right) + \alpha_{n4}^e \cosh\left(\frac{\Lambda_e \lambda_n}{L_e} x_e\right) \tag{16}$$

The continuity conditions for displacement, slope, bending moment, and shear force at the joint between two consecutive elements i and j are, respectively:

$$\psi_n^i(L_i) = \psi_n^j(0) \tag{17}$$

$$\psi_n^{i\prime}(L_i) = \psi_n^{j\prime}(0) \tag{18}$$

$$\Gamma_i \psi_n^{i\prime\prime}(L_i) = \Gamma_j \psi_n^{j\prime\prime}(0) \tag{19}$$

$$\Gamma_i \psi_n^{i\prime\prime\prime}(L_i) = \Gamma_j \psi_n^{j\prime\prime\prime}(0) \tag{20}$$

where $\Gamma_e = (EI)_e/(EI)_o$ relates the element bending stiffness to the element with minimum dynamic stiffness. These conditions along with the boundary constraints define a nonlinear system of equation $T(\lambda)v = 0$, which is solved using the infinite Arnoldi method [19]. The problem is classified as a Sum of Products of Matrices and Functions (SMPF) [20], with a nonlinear eigenvalue problem formulated as:

$$T(\lambda) = \sum_{e}^{N_e} \sum_{i}^{N_{bc}} A_i^e f_i^e(\lambda, \Lambda_e) \tag{21}$$

where, A_i^e are $4N_e \times 4N_e$ matrices, and f_i^e are trigonometric and hyperbolic functions that define N_{bc} boundary constraints. The solution to this problem are the eigenpairs (λ_n^e, v_n^e), with $v_n^e = \{\alpha_{n1}^e, \alpha_{n2}^e, \alpha_{n3}^e, \alpha_{n4}^e\}$, and the natural frequency is $\omega_n = \lambda_n^2 \sqrt{\widetilde{K}_0}$.

The modal mass is obtained as:

$$M_n = \int_0^L |\psi_n(x)|^2 \mu \, dx = \int_0^L \sum_{e=1}^{N_e} |\psi_n^e(x)|^2 \mathbb{1}_{\mathcal{L}_e}(x) \mu \, dx = \sum_{e=1}^{N_e} M_n^e. \tag{22}$$

An analytical solution for M_n^e is given in Appendix A.

The continuity conditions defined by Eqs. (17–20) allow for the appropriate definition of boundary constraints, as well as force equilibrium and displacement continuity between elements. For instance, a pinned support condition is defined by imposing null displacement and bending moment; a fixed support by imposing null displacement and rotation; and a free end by imposing null bending moment and shear force. Similarly, continuity of displacements, rotations, bending moments and shear forces is enforced in spans represented by multiple elements, such as in stepped beams.

2.3. Analytical solution to the normal coordinate equation

The time-domain solution for Eq. (12) can be expressed using the convolution integral:

$$Y_n(t) = (P_n * h_n)(t) = \int_0^t P_n(\tau) h_n(t-\tau) \, d\tau \tag{23}$$

Here $h_n(t-\tau)$ is the unit-impulse response function defined as:

$$h_n(t-\tau) = \frac{1}{M_n \omega_{Dn}} \sin(\omega_{Dn}(t-\tau)) \exp(-\zeta_n \omega_n (t-\tau)) \tag{24}$$

where $\omega_{Dn} = \omega_n \sqrt{1-\zeta_n^2}$ is the damped natural frequency.

Eq. (23) is rewritten according to Eqs. (10) and (14) as follows:

$$Y_n(t) = \sum_{e=1}^{N_e} \int_0^t P_0 \psi_n^e(V\tau) \mathbb{1}_{\mathcal{L}_e}(V\tau) h_n(t-\tau) \, d\tau \tag{25}$$

The impulse response function is expanded according to Clough and Penzien [21]:

$$h_n(t-\tau) = \frac{1}{M_n \omega_{Dn}} \left[\sin(\omega_{Dn} t) \cos(\omega_{Dn} \tau) - \cos(\omega_{Dn} t) \sin(\omega_{Dn} \tau) \right] \exp(-\zeta_n \omega_n t) \exp(\zeta_n \omega_n \tau) \tag{26}$$

This form separates the time-dependent sinusoidal components ($\sin(\omega_{Dn} t)$ and $\cos(\omega_{Dn} t)$) from the input-dependent terms ($\sin(\omega_{Dn} \tau)$ and $\cos(\omega_{Dn} \tau)$):

$$Y_n(t) = \left[A_n(t) \sin(\omega_{Dn} t) - B_n(t) \cos(\omega_{Dn} t) \right] \exp(-\zeta_n \omega_n t) \tag{27}$$

$A_n(t)$ and $B_n(t)$ are time-dependent coefficients given by the modal force:

$$\begin{aligned} A_n(t) &= \frac{1}{M_n \omega_{Dn}} \int_0^t P_n(\tau) \cos(\omega_{Dn} \tau) \exp(\zeta_n \omega_n \tau) \, d\tau \\ &= \frac{P_0}{M_n \omega_{Dn}} \sum_{e=1}^{N_e} \int_0^t \psi_n^e(V\tau) \mathbb{1}_{\mathcal{L}_e}(V\tau) \cos(\omega_{Dn} \tau) \exp(\zeta_n \omega_n \tau) \, d\tau \end{aligned} \tag{28}$$

$$\begin{aligned} B_n(t) &= \frac{1}{M_n \omega_{Dn}} \int_0^t P_n(\tau) \sin(\omega_{Dn} \tau) \exp(\zeta_n \omega_n \tau) \, d\tau \\ &= \frac{P_0}{M_n \omega_{Dn}} \sum_{e=1}^{N_e} \int_0^t \psi_n^e(V\tau) \mathbb{1}_{\mathcal{L}_e}(V\tau) \sin(\omega_{Dn} \tau) \exp(\zeta_n \omega_n \tau) \, d\tau \end{aligned} \tag{29}$$

This procedure eliminates the need to explicitly solve the differential Eq. (12). By expressing the solution in terms of the convolution integral and decomposing the impulse response into its sinusoidal components, the response $Y_n(t)$ can be directly calculated from Eq. (27). The time-dependent coefficients $A_n(t)$ and $B_n(t)$ are derived by integrating the modal force using the expressions given in Eqs. (28) and (29). The coefficient computation involves integrals of trigonometric, hyperbolic, and exponential functions. Thus, the coefficient $A_n(t)$ is expressed as the sum of four integrals:

$$A_n(t) = \frac{P_0}{M_n \omega_{Dn}} \sum_{e=1}^{N_e} \left[\alpha^e_{n1} I^e_{n1}(t) + \alpha^e_{n2} I^e_{n2}(t) + \alpha^e_{n3} I^e_{n3}(t) + \alpha^e_{n4} I^e_{n4}(t) \right] \tag{30}$$

where:

$$I^e_{n1}(t) = \int_0^t \sin\left(\frac{\lambda^e_n V\tau}{L_e}\right) \mathbb{1}_{\mathcal{L}_e}(V\tau) \cos(\omega_{Dn}\tau) \exp(\zeta_n \omega_n \tau)\, d\tau \tag{31a}$$

$$I^e_{n2}(t) = \int_0^t \cos\left(\frac{\lambda^e_n V\tau}{L_e}\right) \mathbb{1}_{\mathcal{L}_e}(V\tau) \cos(\omega_{Dn}\tau) \exp(\zeta_n \omega_n \tau)\, d\tau \tag{31b}$$

$$I^e_{n3}(t) = \int_0^t \sinh\left(\frac{\lambda^e_n V\tau}{L_e}\right) \mathbb{1}_{\mathcal{L}_e}(V\tau) \cos(\omega_{Dn}\tau) \exp(\zeta_n \omega_n \tau)\, d\tau \tag{31c}$$

$$I^e_{n4}(t) = \int_0^t \cosh\left(\frac{\lambda^e_n V\tau}{L_e}\right) \mathbb{1}_{\mathcal{L}_e}(V\tau) \cos(\omega_{Dn}\tau) \exp(\zeta_n \omega_n \tau)\, d\tau \tag{31d}$$

Similarly, $B_n(t)$ is expressed as:

$$B_n(t) = \frac{P_0}{M_n \omega_{Dn}} \sum_{e=1}^{N_e} \left[\alpha^e_{n1} J^e_{n1}(t) + \alpha^e_{n2} J^e_{n2}(t) + \alpha^e_{n3} J^e_{n3}(t) + \alpha^e_{n4} J^e_{n4}(t) \right] \tag{32}$$

where:

$$J^e_{n1}(t) = \int_0^t \sin\left(\frac{\lambda^e_n V\tau}{L_e}\right) \mathbb{1}_{\mathcal{L}_e}(V\tau) \sin(\omega_{Dn}\tau) \exp(\zeta_n \omega_n \tau)\, d\tau \tag{33a}$$

$$J^e_{n2}(t) = \int_0^t \cos\left(\frac{\lambda^e_n V\tau}{L_e}\right) \mathbb{1}_{\mathcal{L}_e}(V\tau) \sin(\omega_{Dn}\tau) \exp(\zeta_n \omega_n \tau)\, d\tau \tag{33b}$$

$$J^e_{n3}(t) = \int_0^t \sinh\left(\frac{\lambda^e_n V\tau}{L_e}\right) \mathbb{1}_{\mathcal{L}_e}(V\tau) \sin(\omega_{Dn}\tau) \exp(\zeta_n \omega_n \tau)\, d\tau \tag{33c}$$

$$J^e_{n4}(t) = \int_0^t \cosh\left(\frac{\lambda^e_n V\tau}{L_e}\right) \mathbb{1}_{\mathcal{L}_e}(V\tau) \sin(\omega_{Dn}\tau) \exp(\zeta_n \omega_n \tau)\, d\tau \tag{33d}$$

The closed-form solution for these integrals is included in Appendix B, involving trigonometric, hyperbolic, and exponential functions. This closed-form solution simplifies the analysis by avoiding numerical integration while maintaining analytical precision and clarity.

Higher-order derivatives of the normal coordinate are obtained by differentiating the convolution integral Eq. (23). For example, the second derivative is:

$$\ddot{Y}_n(t) = (P_n * \ddot{h}_n)(t) + P_n(t)\dot{h}_n(0) \tag{34}$$

and following an expansion similar to Eq. (26) it can be rewritten as follows:

$$\begin{aligned} \ddot{Y}_n(t) = \Big\{ & \left[(-\omega^2_{Dn} + \zeta^2_n \omega^2) A_n(t) - 2\omega_{Dn} \zeta^2_n \omega^2 B_n(t)\right] \sin(\omega_{Dn} t) - \\ & \left[-2\omega_{Dn} \zeta^2_n \omega^2 A_n(t) + (\omega^2_{Dn} - \zeta^2_n \omega^2) B_n(t)\right] \cos(\omega_{Dn} t) \Big\} \exp(-\zeta_n \omega_n t) + \omega_{Dn} P_n(t) \end{aligned} \tag{35}$$

Eqs. (27) and (35) are the analytical solutions for the displacement and acceleration of the normal coordinate $Y_n(t)$ in terms of the time-dependent coefficients $A_n(t)$ and $B_n(t)$ previously defined in Eqs. (30) and (32).

2.4. Time discrete analysis based on sinc interpolation

The time-domain solution can be significantly improved by applying the Whittaker-Shannon interpolation formula or sinc interpolation. This approach is based on the Nyquist-Shannon sampling theorem for reconstructing a band-limited continuous signal from discrete samples.

The Fourier Transform of the normal coordinate is:

$$\mathcal{F}(Y_n)(\omega) = \int_{-\infty}^{+\infty} Y_n(t) \exp(-\imath \omega t)\, dt \tag{36}$$

where the imaginary unit number is denoted by the Greek letter $\imath$ to avoid confusion with the subscripts used in other derivations. The normal coordinate $Y_n(t)$ is band limited by the frequency Ω if the Fourier Transform $\mathcal{F}(Y_n)(\omega) = 0$, $\omega \notin [-\Omega, \Omega]$.

Then, $Y_n(t)$ can be exactly reconstructed from a time-series $\text{Ш}_{\Delta t} Y_n(t) = \{\dots, Y_n(t_{-1}), Y_n(t_0), Y_n(t_1), \dots\}$ with a sampling frequency $f_s = 1/\Delta t$ higher than twice the band limit Ω as follows:

$$Y_n(t) = \text{Ш}_{\Delta t} Y_n * \operatorname{sinc}(t) \tag{37}$$

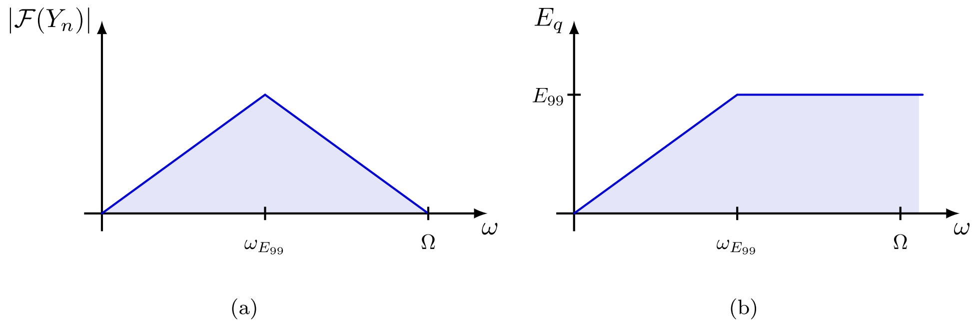

Fig. 1. (a) Fourier transform and (b) energy distribution of a band-limited function.

Table 1
Algorithm for time-discrete analysis using sinc interpolation.

Algorithm Steps	
1.	Modal analysis
	(a) Define a multi-span beam by N_e elements.
	(b) Impose element continuity and boundary constraints (Eqs. (17)–(20)).
	(c) Solve the nonlinear system of equations $T(\lambda)v = 0$.
	(d) Evaluate modal mass (Eq. (22)).
2.	For each mode shape:
	(a) Determine the band limit Ω and low sampling frequency fs.
	(b) Evaluate normal coordinate $\text{III}_{\Delta t}Y_n$ at discrete time (Eqs. (27) and (35)).
	(c) Reconstruct continuous (resampled) solution $Y_n(t)$ using sinc interpolation (Equation (40)).
	(d) Compute modal contribution (Eq. (7)).

where $\text{sinc}(t) = \sin(t)/t$ is the sinc function and $\text{III}_{\Delta t}$ is the shah function:

$$\text{III}_{\Delta t}Y_n(t) = \sum_{k=-\infty}^{\infty} \delta(t - k\Delta t)Y_n(k\Delta t) \tag{38}$$

Eq. (37) can be efficiently computed using the Fast Fourier Transform (FFT) of $Y_n(t)$. It should be noted that $\mathcal{F}(Y_n)$ coincides with the discrete spectrum $\mathcal{F}(\text{III}_{\Delta t}Y_n)$ in the frequency range $[-\Omega, \Omega]$, and the inverse Fourier transform of the discrete spectrum does not change if it is zero padded:

$$\mathcal{F}(\text{III}_{\Delta t}Y_n\Pi_\Omega) = \begin{cases} \mathcal{F}(\text{III}_{\Delta t}Y_n) & \omega \in [-\Omega, \Omega] \\ 0 & \omega \notin [-\Omega, \Omega] \end{cases} \tag{39}$$

Thus, the solution $Y_n(t)$ can be reconstructed from a time-series according to Eq. (37) by the inverse Discrete Fourier Transform:

$$Y_n(t) = \text{III}_{\Delta t}Y_n * \text{sinc}(t) = \mathcal{F}^{-1}(\text{III}_{\Delta t}Y_n\Pi_B) \tag{40}$$

Therefore, the normal coordinate $Y_n(t)$ can be resampled from a time series evaluated at a low sampling frequency f_s to a higher resolution $\hat{f}_s$ by zero-padding the frequency spectrum. The size of $\mathcal{F}(\text{III}_{\Delta t}Y_n\Pi_\Omega)$ must be increased to $\hat{f}_s/f_s$ times the original series length. The sampling rate f_s must be at least twice the band limit Ω to ensure accurate time-discrete analysis without aliasing according to the Nyquist-Shannon sampling theorem.

Fig. 1(a) shows a representation of the Fourier transform of a band-limited function. The shaded region represents the spectrum extending up to the band limit Ω. For negative frequencies, the distribution is conjugate symmetric. The band limit can be determined from the energy in $Y_n(t)$ using the Parseval's theorem. Thus, the centre frequency $\omega_{E_{99}}$ is defined as the frequency for which the percentile E_{99} of the total energy is obtained (Fig. 1(b)):

$$E_{99} = \frac{1}{2\pi}\int_{-\omega_{E_{99}}}^{+\omega_{E_{99}}} |\mathcal{F}(Y_n)(\omega)|^2 \, d\omega = 0.99\left(\frac{1}{2\pi}\int_{-\infty}^{+\infty} |\mathcal{F}(Y_n)(\omega)|^2 \, d\omega\right) \tag{41}$$

The proposed time-discrete analysis based on sinc interpolation enhances computational efficiency while maintaining analytical accuracy, provided that the sampling rate satisfies the Nyquist-Shannon theorem. A time series $\text{III}_{\Delta t}Y_n$ with a low sampling frequency is analytical without the need for a time integration scheme. Table 1 summarised the algorithm for time-discrete analysis using sinc interpolation.

3. Response of multi-span beams under moving loads

In this section, four application examples are presented to illustrate the proposed methodology.

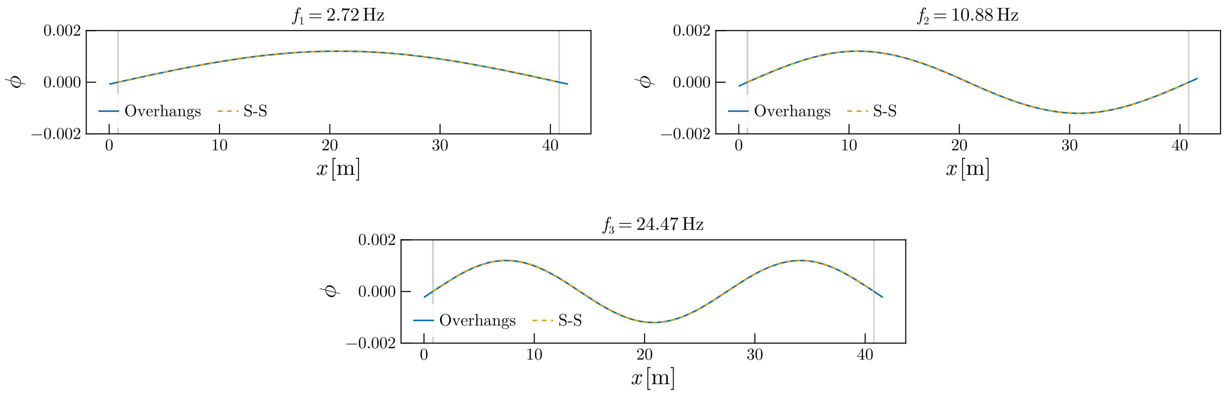

Fig. 2. Mode shapes for a single-span bridge with overhangs (Overhangs) and for a simply-supported configuration (S-S). Vertical solid grey lines delimit the abutment locations.

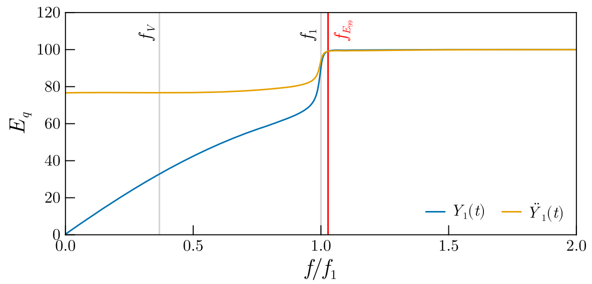

Fig. 3. Energy percentile for a single-span bridge with overhangs due to a moving load at $V = 80$ m/s.

3.1. Example 1: single-span bridge with overhangs

In the first example, a railway bridge from the Madrid-Barcelona high-speed line in Spain is considered. It is a single-span bridge simply-supported (S-S) with a total length of $L = 40$ m and overhangs of 0.8 m at both ends. The bridge properties are Young's modulus $E = 30.9$ GPa, cross-section moment of inertia $I = 8.59\,\mathrm{m}^4$ and mass per unit length $\mu = 34610$ kg/m. The assigned modal damping is $\zeta_n = 0.01$.

The beam is modelled by three elements of length $L_e = \{0.8, 40.0, 0.8\}$ m to represent the single-span and the overhangs. The continuity conditions for displacement, rotation, and bending moment are imposed between elements according to Eqs. (17)– (19). Additionally, the free-end condition at the overhangs is enforced by setting the bending moment and shear force to zero.

These conditions define a system of $4N_e$ homogeneous equations for determining the eigenvalues and their corresponding eigenvectors, which have $4N_e$ components. It should be noted that the system becomes overdetermined if shear continuity is also imposed. The continuity of shear forces between elements is ensured, as the mode shape given by Eq. (16) has C^n continuity.

The resulting mode shapes and eigenfrequencies correspond to those of a simply-supported beam, as shown in Fig. 2, indicating that the overhangs had a negligible effect on the overall dynamic response due to their small mass contribution. The mode shapes were normalised to the modal mass, $\phi_n = \psi_n/\sqrt{M_n}$.

The discrete-time analysis is performed by identifying the bandwidth in which the modal contribution is significant. Fig. 3 shows the energy percentile in the normal coordinate of the first mode shape due to a unit single load at a speed $V = 80$ m/s for displacement and acceleration. The excitation frequency of the moving load $f_V = V/L$, the first natural frequency, and the frequency corresponding to the energy percentile $f_{E_{99}}$ are shown in Fig. 3. The centre frequency is given by $f_{E_{99}}$ (see Fig. 1), which is 1.35 times the first natural frequency. The bandwidth is estimated as $\Omega = 2f_{E_{99}}$.

The contribution of the first mode is obtained by evaluating Eqs. (27) and (35) at discrete time intervals with a sampling frequency $f_s = 2.56\Omega$, ensuring that the Nyquist frequency is at least twice the band limit. The discrete sample size is set to $N = 1024$, a power of 2, to optimise the FFT algorithm. The solution is then resampled at a high sampling rate $\hat{f}_s = 20f_1$.

Fig. 4(a and b) show the time response for the modal solution and its second derivative, computed at both low and high sampling rates, along with the resampled results computed from low sampling solution according to Eq. (40). The dots mark the samples computed at a low frequency rate which coincide with the solution obtained at high sampling rate. The resampled data are in perfect agreement with the high sampling rate solution. Note that the high sampling rate is used for comparison purposes only, and its selection is arbitrary.

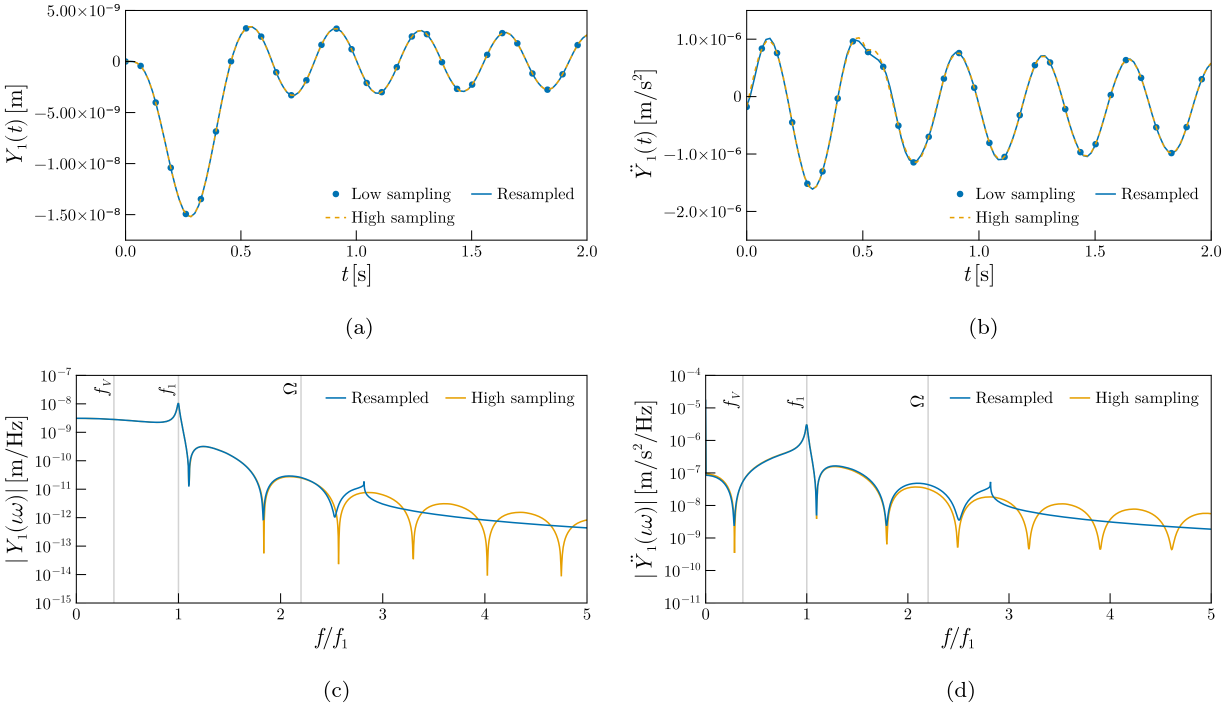

Fig. 4. (a,b) Time response and (c,d) frequency content of the first normal coordinate for a single-span bridge with overhangs under a moving load at $V = 80\,\text{m/s}$.

3.2. Example 2: three-span bridge with oversails

The second example is a bridge on the Mälarbanan railway line in Sweden. This structure is a three-span continuous bridge with two piers and two abutments with oversails. The span lengths are $L_e = \{17.4,\ 20.3,\ 19.3\}$ m. The bridge properties are characterised by Young's modulus $E = 34\,\text{GPa}$, cross-section moment of inertia $I = 1.513\,\text{m}^4$ and mass per unit length $\mu = 18680\,\text{kg/m}$. The modal damping is $\zeta_n = 0.01$.

The oversails are represented by two additional spans of length 2 m with clamped boundary conditions at both ends. This condition partially constrains the rotation of the initial and last spans. The number of elements is set to $N_e = 5$. The mode shapes show slight differences compared to the fixed support configuration, as shown in Fig. 5(a and b). The natural frequencies are slightly lower compared to the fixed-end configuration, with maximum differences of 4 %.

Fig. 5 shows the frequency content of the modal solution for acceleration and the cumulative energy of the first and second mode shapes, obtained for a single unit load travelling at $V = 80\,\text{m/s}$. The spectrum shows dominant peaks corresponding to the natural frequency and the excitation frequency of the load, estimated as $f_V = (\lambda_n^e / L_e) V / 2\pi$. The frequency value is the same for all elements, regardless the element length and eigenvalue. The frequency corresponding to the energy percentile E_{99} is ten percent higher than the natural frequency for both mode shapes. The response is band-limited at $\Omega = 2 f_{E_{99}}$, beyond which the frequency content decays rapidly. The resampled spectrum is well represented, with only minor deviations at frequencies close to Ω. Therefore, the choice of the low-frequency rate $f_s = 2.56\Omega = 2.56(1.1 f_n)$ was accurate compared to the solution evaluated at a high sampling rate $\hat{f}_s = 20 f_n$.

3.3. Example 3: 7-span bridge with in-span hinges

The second example is a cantilever-suspended girder bridge [22]. This structure is a seven-span bridge with a total length of $L = 186.4\,\text{m}$ and pinned-pinned boundary conditions at both ends. The bridge comprises seven beams of lengths $L = \{16.0,\ 40.4,\ 16.0,\ 40.4,\ 16.0,\ 40.4,\ 16.0\}$ m connected by in-span hinges. This configuration gives seven spans of constant length 22.2 m. It is a composite deck structure with equivalent properties defined by Young's modulus $E = 57.4\,\text{GPa}$, cross-section moment of inertia $I = 0.245\,\text{m}^4$ and mass per unit length $\mu = 5376.7\,\text{kg/m}$. The modal damping is $\zeta_n = 0.01$.

The bridge was modelled by 13 elements of length $L_e = \{16.0,\ 6.2,\ 28.4,\ 6.2,\ 16.0,\ 6.2,\ 28.4,\ \text{SYM}\}$ m with a symmetric configuration to represent the supports and the in-span hinges. The continuity conditions for displacement, bending moment, and shear force is imposed between elements connected by the hinges. Fig. 6 shows the first and second mode shapes, characterised by discontinuities in the slope at the in-span hinges.

The response produced by a unit moving load travelling at a velocity of $V = 40\,\text{m/s}$ is complex. The frequency content is widely distributed and does not decay as in previous cases. Therefore, the percentile E_{99} is obtained for frequencies approximately 60 %

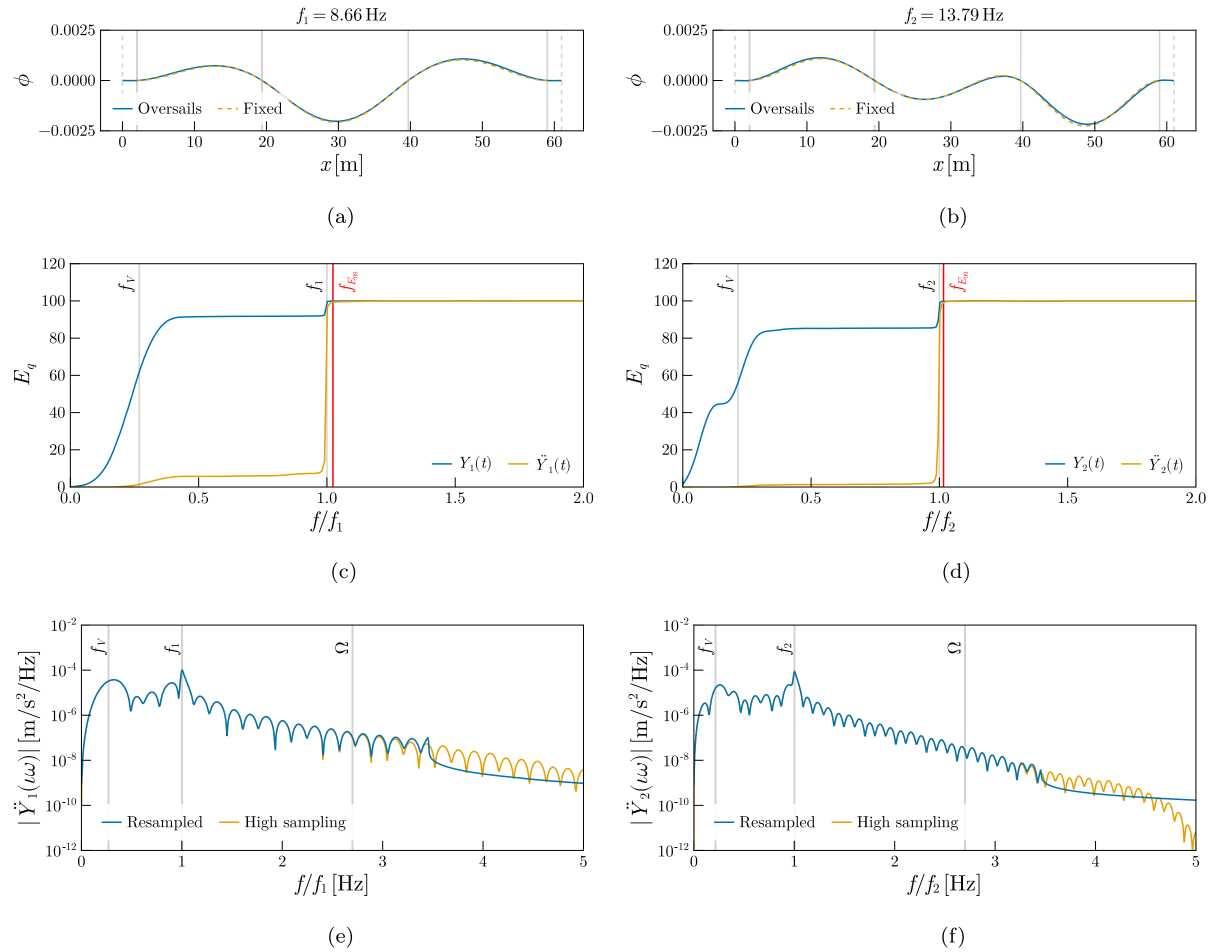

Fig. 5. (a,b) Mode shapes for a three-span bridge with oversails. Vertical grey lines delimit the span positions and dashed lines the oversails ends. (c,d) Energy percentile and (e,f) normal coordinate of the acceleration due to a moving load travelling at $V = 80\,\mathrm{m/s}$.

higher than the first and second natural frequencies, $f_{E_{99}} = 1.6 f_n$. Thus, the band limit equals $\Omega = 2 f_{E_{99}}$ and the low sampling rate $f_s = 2.56\Omega = 8.2 f_n$. The high $f_{E_{99}}$ value indicates that the response is not well band-limited in this case. However, the agreement between the resampled solution and the exact solution computed at a high sampling rate is good. The accuracy could be further improved by increasing the sampling rate.

3.4. Example 4: 28-span bridge under train loads

In the last case study, a bridge on the Erfurt-Leipzig/Halle high-speed railway line in Germany is examined. This structure is a 28-span bridge with a total length of $L = 1104\,\mathrm{m}$ and pinned-pinned boundary conditions at both ends. The span lengths are given by $L_e = \{43,\ 6\times 44,\ 9\times 30,\ 11\times 44,\ 43\}$ [m]. The bridge properties are characterised by a Young's modulus of $E = 30\,\mathrm{GPa}$, a moment of inertia of $I = 18.875\,\mathrm{m}^4$ and a mass per unit length of $\mu = 45860\,\mathrm{kg/m}$. The modal damping ratio is set to $\zeta_n = 0.01$.

In this example, the structural response is calculated for the passage of the HSLM-A1 train model [7]. The train load model consists of $N_l = 50$ axles with a distribution of axle loads and spacing, as shown in Fig. 7(a). The solution for the train load was obtained from the superposition of N_l single loads with amplitudes $P_{0,l}$ and time shifts σ_l. The longitudinal distribution of the axle loads through the rails and sleepers was considered according to the specifications in ref. [7].

Although the solution can be computed by evaluating the response to a single load and then applying successive time shifts, for example using the properties of the FFT, it is computationally more efficient to calculate the modal solution at a low sampling rate and then resample the response at a higher frequency. Thus, the normal coordinate is expressed as:

$$Y_n(t) = \sum_{l=1}^{N_l} \left[(P_{n,l} * h_n)(t) \right] = \sum_{l=1}^{N_l} \left[\int_0^t P_{n,l}(\tau - \sigma_l) h_n(t-\tau)\, d\tau \right] \tag{42}$$

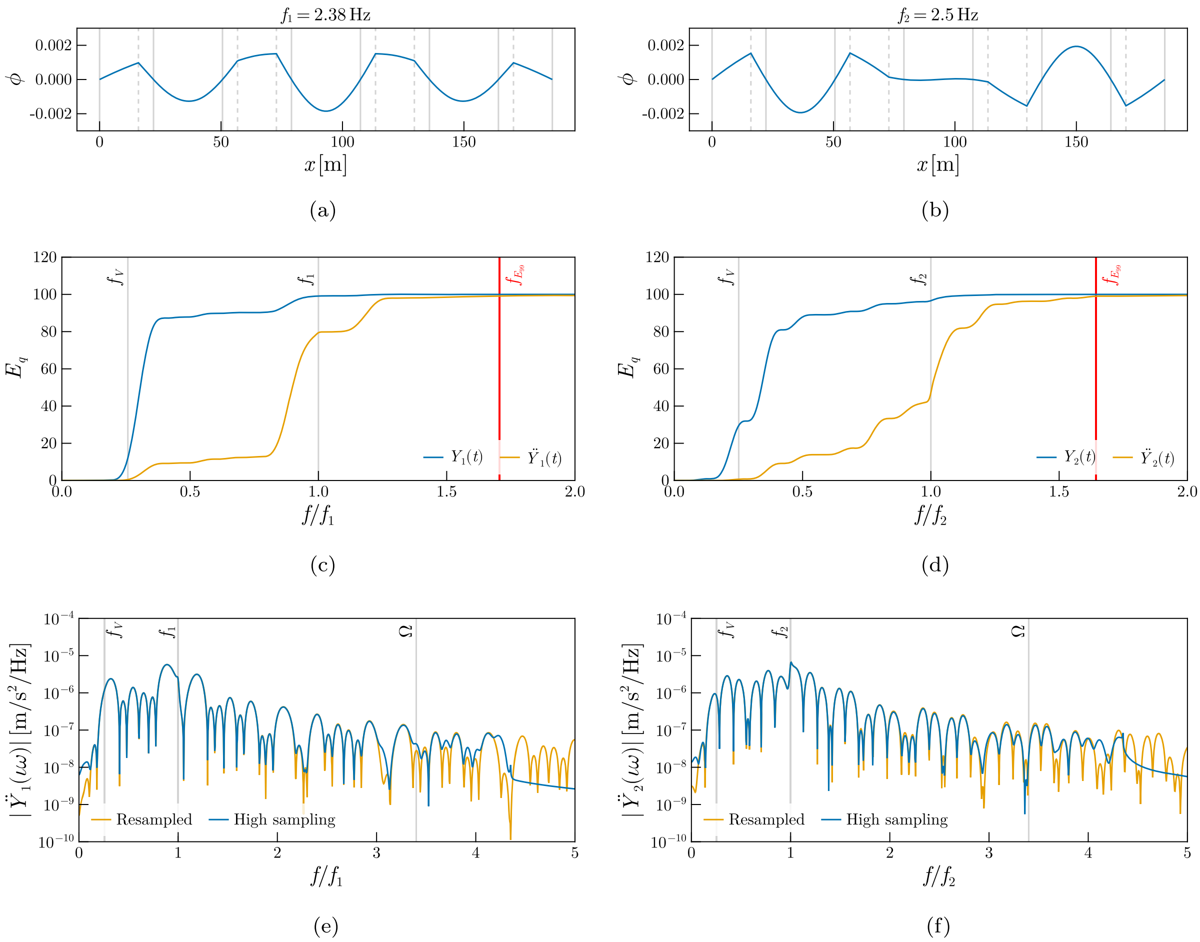

Fig. 6. (a,b) Mode shapes for a 7-span bridge with in-span hinges. Vertical grey lines delimit the span positions and dashed lines the in-span hinge locations. (c,d) Energy percentile and (e,f) normal coordinate of the acceleration due to a moving load with $V = 40\,\mathrm{m/s}$.

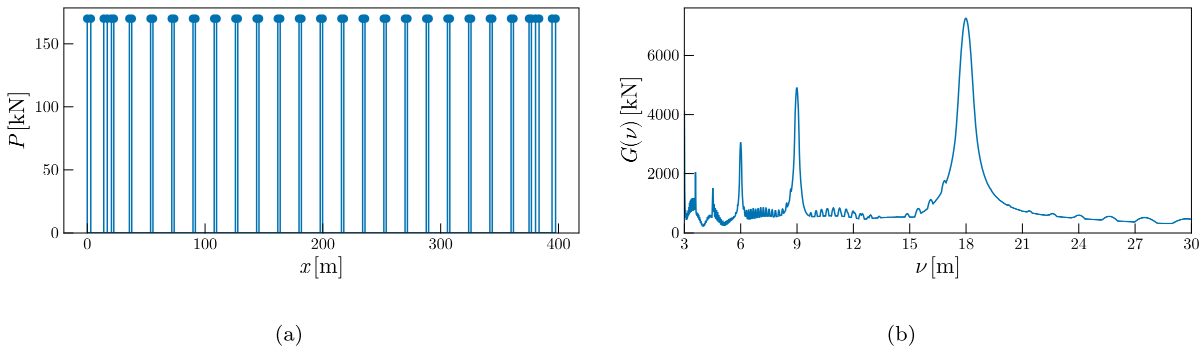

Fig. 7. (a) Load distribution and (b) dynamic train signature for the HSLM-A1 model.

where $P_{n,l}$ represents the modal force for the load with amplitude $P_{0,l}$. The train excitation frequency is now considered to determine the band limit according to the train dynamic signature $G(\nu)$ [23]:

$$G(\nu) = \max_{l=1}^{N_l} \left\{ \left[\sum_{1 \leq k \leq l} P_k \cos(2\pi\delta_k) \exp(-2\pi\delta_k) \right]^2 + \left[\sum_{1 \leq k \leq l} P_k \sin(2\pi\delta_k) \exp(-2\pi\delta_k) \right]^2 \right\}^{1/2} \tag{43}$$

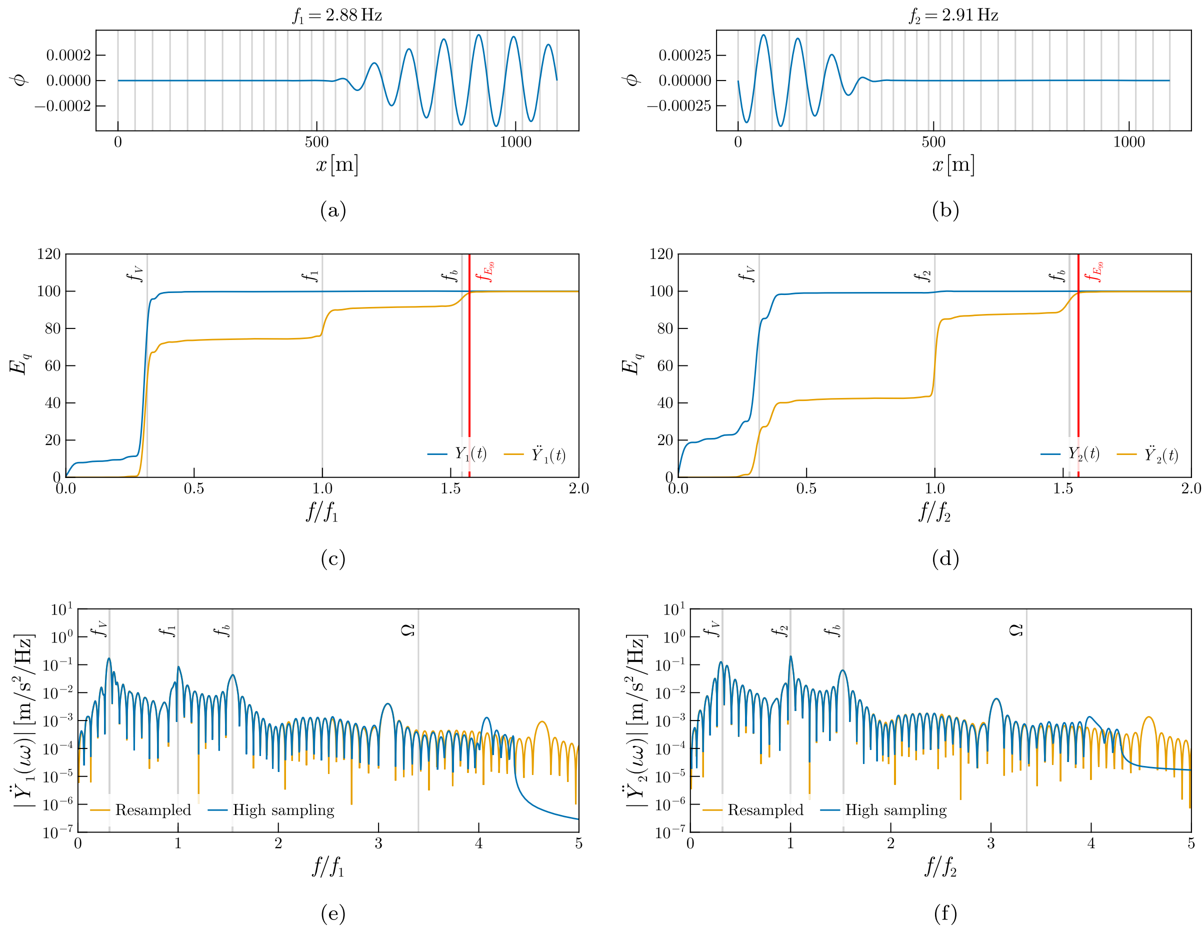

Fig. 8. (a,b) Mode shapes of a 28-span bridge. Vertical grey lines delimit the span supports. (c,d) Energy percentile and (e,f) normal coordinate of the acceleration due to a moving load at $V = 80\,\text{m/s}$.

where P_k is the load amplitude of the k-th axle and $\delta_k = (x_k - x_1)/\nu$, ν being the wavelength and $x_k = 1, \dots, N_l$. The HSLM-A1 train has a characteristic wavelength $\nu_b = 18\text{m}$ (Fig. 7(b)), which defines the bogie passing frequency $f_b = V/\nu_b$.

Fig. 8 shows the first and second modes, which correspond to the modal contributions at the last and first spans, respectively. The spectrum shows dominant peaks related to the natural frequency, load frequency f_V, bogie passing frequency f_b, and higher harmonics. The energy percentile E_{99} is determined at the bogie passing frequency. The resampled spectrum accurately represents the response, with only minor deviations at frequencies close to Ω.

Fig. 9 shows the last span bridge response obtained from Eq. (7). The response was calculated by considering the contribution of 61 mode shapes below 30 Hz. Eq. (42) is evaluated at a low sampling rate with a band limit given for each mode. The response is then resampled at a higher frequency $\hat{f} = 600\,\text{Hz}$ before the mode superposition, significantly reducing the computational effort. The agreement between the resampled and exact solutions at a high sampling rate validates the proposed method.

3.5. Discussion: band limit and low sampling rate

The results indicate that the bandwidth of the normal coordinate Y_n and its second derivative $\ddot{Y}_n$ exceed the load frequency f_V, natural frequency f_n, and the bogie passage frequency f_b. The band limit was defined as $\Omega = 2f_{E_{99}}$ using the energy percentile E_{99}, where $f_{E_{99}}$ varies depending on the complexity of the response.

For simple configurations, such as single-mode responses excited by a moving load, the frequency $f_{E_{99}}$ is typically close to the natural frequency, with $f_{E_{99}} \approx 1.1 \times \max\{f_V, f_n, f_b\}$. In these cases, the response is band-limited, and a low sampling rate of $f_s = 2.56\Omega$ ensures accuracy in the resampled solution. However, for more complex configurations, such as Example 3.3, the frequency content of the normal coordinate is widely distributed, and the frequency percentile $f_{E_{99}}$ increases significantly.

Thus, while a standard criterion of $f_{E_{99}} \geq 1.1 \times \max\{f_V, f_n, f_b\}$ is sufficient for well-band-limited responses, higher sampling rates are required in complex multi-span beam configurations to ensure accuracy.

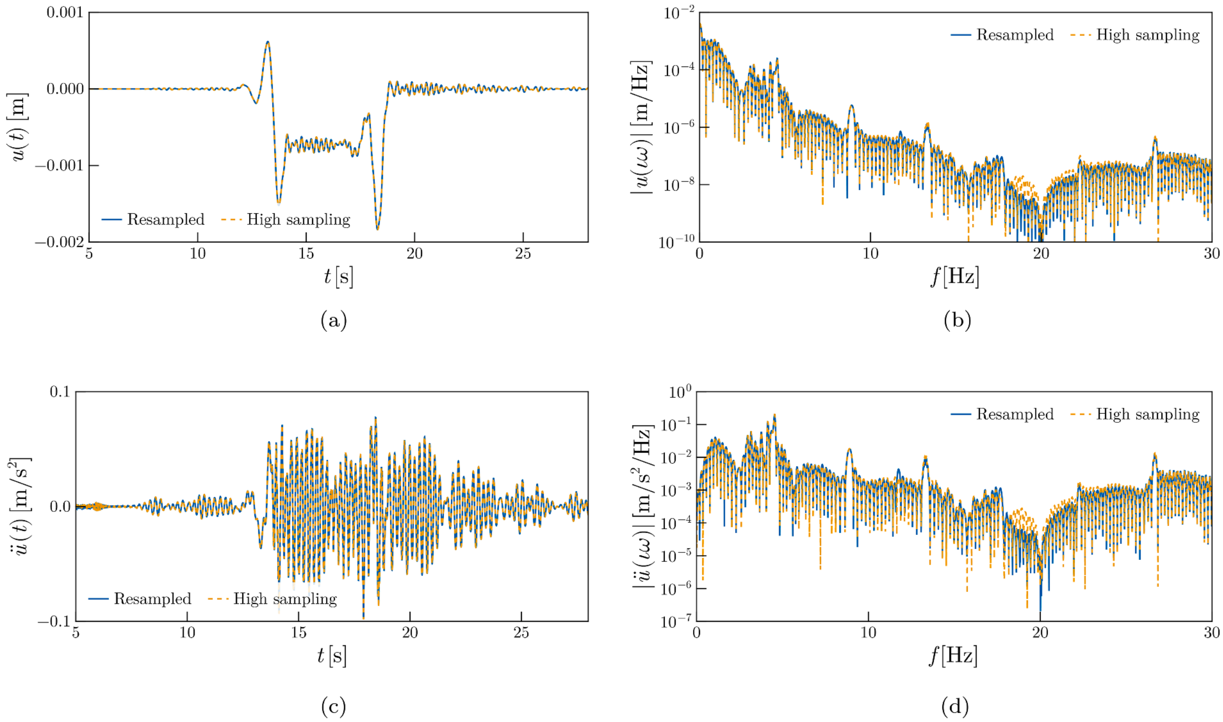

Fig. 9. Displacement and acceleration at midpoint of the last span of a 28-span bridge for the HSLM-A1 train model travelling at $V = 80\,\mathrm{m/s}$.

Table 2
Benchmark analysis and performance comparison for computing the first normal coordinate and the bridge response for HSLM-A1 passage at speed $V = 80\,\mathrm{m/s}$.

Method	First normal coordinate			Bridge response		
	CPU time	**Allocations**	**Memory**	**CPU time**	**Allocations**	**Memory**
Time discrete analysis	6.407 ms	19	39.11 KiB	3.082 s	1300	22.88 MiB
High sampling rate	13.184 ms	0	0 bytes	24.767 s	141	772.312 KiB
Newmark's method	243.527 ms	8,928,900	282.44 MiB	250.727 s	7,041,464,991	216.65 GiB
Bathe's method	661.281 ms	16,244,250	481.75 MiB	520.028 s	12,878,634,291	370.63 GiB

4. Benchmarking quadrature rules

Finally, the performance and accuracy of two quadrature rules for solving the dynamic response under train load are evaluated: *i*) the trapezoidal Newmark-β method and *ii*) the Bathe method based on the trapezoidal rule and the three-point backward Euler method. The benchmark test runs over the 28-span bridge studied in Section 3.4.

Fig. 10(a and b) show the results for displacement and acceleration of the first normal coordinate for an HSLM-A1 passage at speed $V = 80\,\mathrm{m/s}$. The time step is set to $\Delta t = T_1/20$, where T_1 is the fundamental period of the bridge. There is perfect agreement between the analytical solution evaluated at high sampling given by Δt and the resampled results from the time discrete analysis, which does not exhibit the effect of numerical damping and period elongation of the quadrature rules. These effects are more noticeable in the acceleration results of the Newmark's method.

The bridge response at the last span is computed by modal superposition considering mode shapes with natural frequencies lower than $f_{\max} = 30\,\mathrm{Hz}$. The time step for the quadrature rules and all mode shapes is set to $\Delta t = T_{\min}/20$, where $T_{\min} = 1/f_{\max}$. Consequently, the numerical results for low-order mode shapes are computed with more steps per period than those for high-order mode shapes. As the time step is very small for the low-order modes, the numerical results improve, leading to a more accurate approximation of the bridge response, as shown in Fig. 10(c and d).

In Table 2 CPU time, memory allocation, and memory usage of the different integration methods are compared. The proposed time discrete analysis is the fastest method with low memory requirements, although it requires 19 memory allocations for resampling. The high sampling-rate solution (2× slower) does not require memory allocation and avoids memory consumption due to resampling operations. The Newmark-β and Bathe integration methods are computationally expensive (40× and 110× slower, respectively) and require high memory usage. The benchmark analysis for computing the bridge response results in an increase of the CPU time up to 170× for the quadrature rules in comparison with the time discrete analysis, with high use of the heap memory.

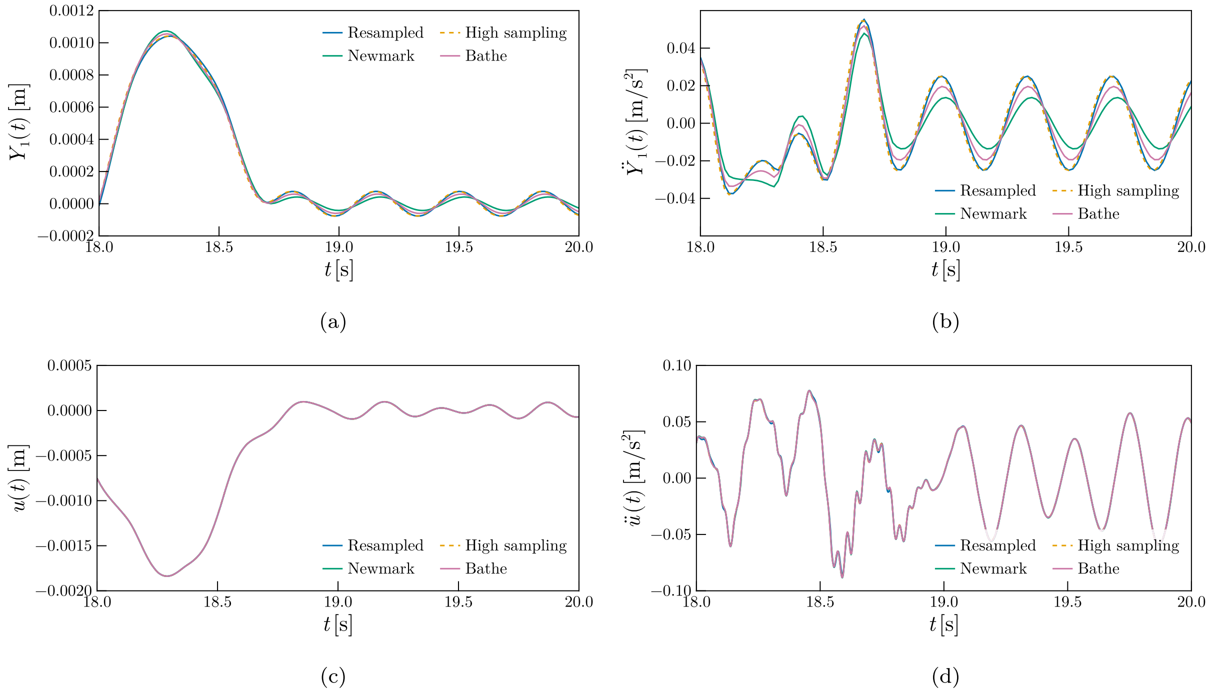

Fig. 10. (a,b) Normal coordinate of the first mode shape and (c,d) displacement and acceleration at the mid-span of the last span of 28-span bridge for the HSLM-A1 train travelling at $V = 80$ m/s.

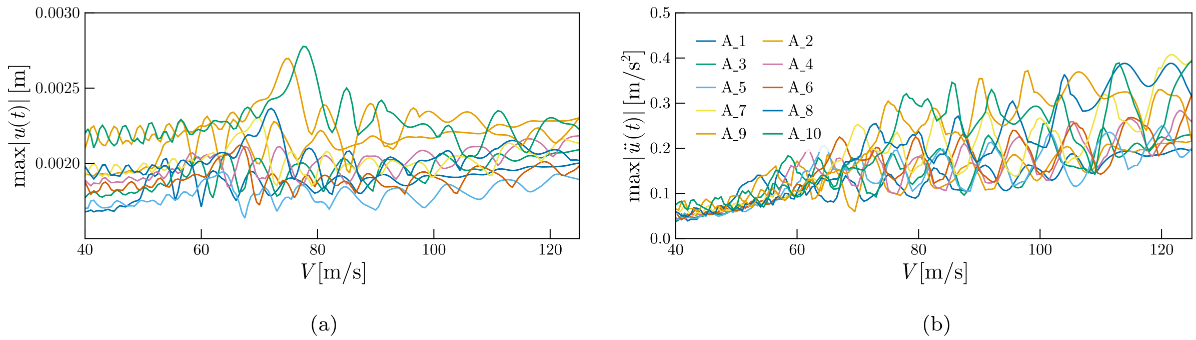

Fig. 11. Envelope of the last span maximum displacement and acceleration for the ten HSLM-A train models.

Fig. 11 shows the envelope for the last span maximum displacement and acceleration for the ten HSLM-A train models over a speed range of 40 m/s to 125 m/s, with 0.5 m/s increments. The computational cost of using the proposed method was 108.2 min for the computation of 1710 cases (171 speeds and 10 train models). The solution to this problem using conventional numerical methods, on the other hand, is not feasible due to the excessive computational cost, which is estimated to be 15 days. This demonstrates the efficiency of the time-discrete analysis, which allows the accurate calculation of bridge responses under moving loads with analytical precision. The advantages of this approach are even more significant when dealing with several cases or considering the contribution of several mode shapes.

5. Extension to finite element models

The proposed methodology can be extended to three-dimensional bridge geometries using finite element (FE) models. Given the FE mode shape ψ_n^q evaluated at points x_q and its corresponding natural frequency ω_n^q, the eigenvalues λ_n^e are obtained according to Eq. (4), while the eigenvectors v_n^e are determined by solving a constrained least-squares problem:

$$\min_{v} \ \frac{1}{2}\|T(\lambda_n)v_n - \psi_n^q\|_2^2 \tag{44}$$

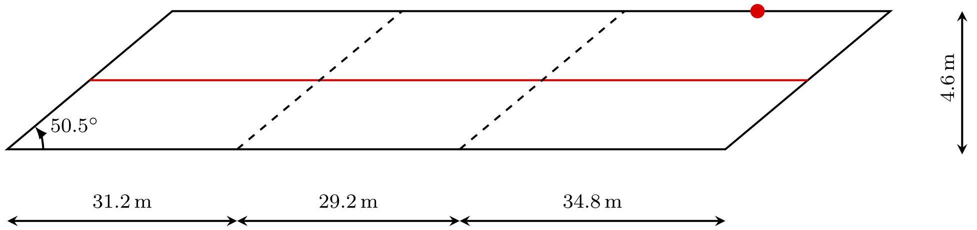

Fig. 12. Plan view of a three-span skewed bridge. Intermediate supports are shown with dashed lines, the loading axis in red, and the observation point is marked by a red circle.

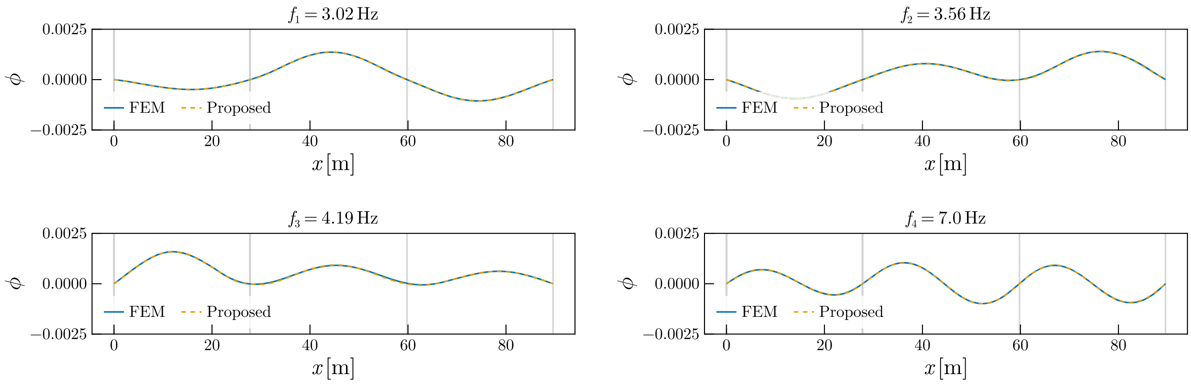

Fig. 13. Mode shapes for a three-span skewed bridge. Vertical solid grey lines delimit the abutment locations.

subject to the linear constraints:

$$C v_n = d \tag{45}$$

where C and d represent the support conditions of the structure. The related Lagrangian function is written as follows:

$$\mathcal{L}(v_n, \nu_n) = \frac{1}{2}\|T(\lambda_n)v_n - \psi_n^q\|_2^2 + \nu_n^\top (C v_n - d) \tag{46}$$

where ν_n are the Lagrange multipliers. The first-order Karush–Kuhn–Tucker (KKT) conditions are given by:

$$\nabla_{v_n}\mathcal{L} = T(\lambda_n)^\top \left(T(\lambda_n)v_n - \psi_n^q\right) + C^\top \nu_n = 0, \tag{47}$$

$$\nabla_{\nu_n}\mathcal{L} = C v_n - d = 0 \tag{48}$$

These conditions lead to the augmented KKT system:

$$\begin{bmatrix} T(\lambda_n)^\top T(\lambda_n) & C^\top \\ C & 0 \end{bmatrix} \begin{bmatrix} v_n \\ \nu_n \end{bmatrix} = \begin{bmatrix} T(\lambda_n)^\top \psi_n^q \\ d \end{bmatrix} \tag{49}$$

The solution of (49) yields the eigenvectors $v_n^e = \{\alpha_{n1}^e, \alpha_{n2}^e, \alpha_{n3}^e, \alpha_{n4}^e\}$. This approach allows the proposed methodology to be extended to more complex bridge geometries while retaining both computational efficiency and accuracy.

5.1. Example

As an example, the results for a bridge on the Paris–Lyon high-speed railway line in France are presented. The structure consists of a three-span continuous bridge with lengths $L_e = \{31.2, 29.2, 34.8\}$ [m] and a skew angle of 50.5°. The deck is an orthotropic slab with a width of 1.1 m and mass per unit length $\mu = 21596$ kg/m. The bridge material properties are characterised by the Young's modulus in the longitudinal direction $E_x = 56.3$ GPa and in the transverse direction $E_y = 30.0$ GPa, the Poisson ratio $\nu_{xy} = 0.2$, and the shear modulus $G_{xy} = 20.5$ GPa. A FE model was developed in `ANSYS` using the orthotropic shell element `SHELL181`. The boundary conditions impose zero longitudinal, transverse, and vertical displacements at the abutments and intermediate supports. A total of 17 mode shapes were identified below 30 Hz, comprising longitudinal and transverse bending modes, as well as torsional modes.

The natural frequencies ω_n^q and mode shapes at the loading axis ψ_n^q resulting from the modal analysis were used to solve Eq. (46). The constraint matrix C and vector d enforce pinned conditions at both the intermediate and end supports. Solving the constrained minimisation problem yielded the eigenpairs (λ_n^e, v_n^e). Fig. 13 compares the first four mode shapes obtained from the FE model with those predicted using the proposed approach, showing an excellent agreement.

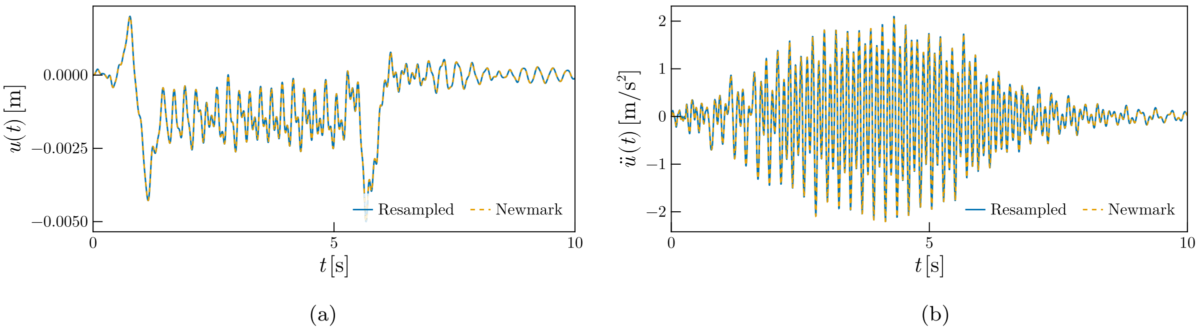

Fig. 14. Displacement and acceleration at the observation point of a three-span skewed bridge for the HSLM-A1 train model travelling at $V = 80\,\mathrm{m/s}$.

Finally, Fig. 14 compares the bridge displacement and acceleration at the observation point defined in Fig. 12. The results obtained with the proposed approach are in very good agreement with those computed from numerical integration of the FE mode shapes, confirming the capability of the method to accurately interface with FE models.

The results presented in this section show that the proposed methodology can be effectively integrated within finite element models to analyse more realistic bridge configurations. This approach provides a powerful method for solving large-scale problems in railway bridge dynamics while maintaining computational efficiency and accuracy. This makes it particularly suitable for parametric studies, optimisation problems, and design verification in high-speed railway lines.

6. Program implementation and availability

The proposed method is implemented in the `SINC-Dyn` function package developed in Julia. The proposed method uses several specialised libraries, including SLEEF [24] and FFTW [25], to optimise the computational performance. SLEEF was used for fast computation of trigonometric and exponential functions, while FFTW was used to perform RFFT (Real-to-Complex FFT) and IRFFT (Inverse Complex-to-Real FFT) versions of the Fast Fourier Transform. Performance analysis was conducted using the StructuralDynamicsODESolvers library [26] for quadrature rules and BenchmarkTools [27] for rigorous benchmarking. The figures in this paper were generated using the Makie library [28].

The `SINC-Dyn` package is available on GitHub under the MIT license (https://github.com/antonioaro/SincBridgeDynamics.jl), ensuring open access and reproducibility of the results.

7. Conclusions

This study presents an efficient analytical method for calculating the dynamic response of multi-span continuous bridges subjected to moving loads. By using time-discrete analysis with sinc interpolation, the proposed approach achieves high analytical accuracy while significantly reducing computational complexity. Unlike conventional numerical methods, which often suffer from numerical damping and period elongation, this method provides explicit closed-form solutions that maintain accuracy with an outstanding reduction of the computational cost.

Through benchmark analyses, the proposed methodology demonstrates superior performance compared to traditional numerical integration techniques, such as the Newmark-β and Bathe methods. The time-discrete analysis outperforms these methods in terms of computational speed and memory efficiency, making it particularly suitable for large-scale simulations involving complex structural models, multiple load cases, and modal contributions. The results confirm that the sinc-based approach eliminates numerical effects and provides a stable and accurate representation of bridge dynamics under moving loads. Moreover, the proposed method can be integrated within finite element models to analyse complex bridge configurations, providing a powerful tool for solving large-scale problems while maintaining computational efficiency and accuracy.

The methodology has been implemented in the open-source Julia package `SINC-Dyn` to facilitate its adoption, which integrates state-of-the-art computational tools to optimise performance. This study ensures reproducibility and encourages further development in the field.

CRediT authorship contribution statement

A. Romero: Writing – original draft, Writing – review & editing, Validation, Supervision, Software, Methodology, Investigation, Funding acquisition, Conceptualization; **E. Moliner:** Writing – original draft, Writing – review & editing, Validation; **M. D. Martínez-Rodrigo:** Writing – original draft, Writing – review & editing, Validation, Funding acquisition; **P. Galvín:** Writing – original draft, Writing – review & editing, Validation, Supervision, Investigation, Funding acquisition.

Data availability

Data will be made available on request.

Declaration of competing interest

The authors declare that they have no known competing financial interests or personal relationships that could have appeared to influence the work reported in this paper.

Acknowledgments

The authors acknowledge the following institutions for their financial support: Spanish Ministry of Science and Innovation, Agencia Española de la Investigación (AEI) and FEDER EU Funds (PID2022-138674OB-C2); and Regional Government of Economic Transformation, Industry, Knowledge and Universities of Andalusia (PROYEXCEL00659). This project has received funding from the Europe's Rail Joint Undertaking under Horizon Europe research and innovation programme under grant agreement no 101121765 (HORIZON-ER-JU-2022-ExplR-02). Views and opinions expressed are however those of the author(s) only and do not necessarily reflect those of the European Union or Europe's Rail Joint Undertaking. Neither the European Union nor the granting authority can be held responsible for them. The authors acknowledge the support of the Andalusian Scientific Computing Centre (CICA).

Appendix A. Element modal mass

Analytical solution for the element modal mass M_n^e in Eq. (22). The element superscript and subscript e are omitted for clarity of notation.

$$\begin{aligned}
M_n &= \int_0^L |\psi_n(x)|^2 \mu \, dx \\
&= \frac{L\mu}{4\lambda_n} \Big\{ 2\lambda_n \left(\alpha_{n1}^2 + \alpha_{n2}^2 - \alpha_{n3}^2 + \alpha_{n4}^2\right) + \\
&4\left[\alpha_{n1}\alpha_{n2}(1-\cos^2(\lambda_n)) - \alpha_{n3}\alpha_{n4}(1-\cosh^2(\lambda_n))\right] + \\
&4\cosh(\lambda)\left[(\alpha_{n2}\alpha_{n3} - \alpha_{n1}\alpha_{n4})\cos(\lambda_n) + (\alpha_{n1}\alpha_{n3} + \alpha_{n2}\alpha_{n4})\sin(\lambda_n)\right] + \\
&2\left(\alpha_{n2}^2 - \alpha_{n1}^2\right)\sin(\lambda_n)\cos(\lambda_n) + \\
&2\sinh(\lambda_n)\left[2(\alpha_{n2}\alpha_{n4} - \alpha_{n1}\alpha_{n3})\cos(\lambda_n) + \left(\alpha_{n3}^2 + \alpha_{n4}^2\right)\cosh(\lambda_n) + 2(\alpha_{n1}\alpha_{n4} + \alpha_{n2}\alpha_{n3})\sin(\lambda_n)\right]\Big\}
\end{aligned} \tag{A.1}$$

Appendix B. Integration of time-dependent coefficients

Analytical solution for indefinite element integrals in time-dependent coefficients (Eqs. (30) and (32)). The element superscript and subscript e are omitted for clarity of notation.

$$A_{n0} = \frac{\lambda_n V}{L}, \quad C_n = \zeta_n \omega_n \tag{B.1}$$

$$A_{n1} = \frac{C_n \sin((A_{n0}+\omega_{Dn})t) - (A_{n0}+\omega_{Dn})\cos((A_{n0}+\omega_{Dn})t)}{C_n^2 + (A_{n0}+\omega_{Dn})^2} \tag{B.2}$$

$$A_{n2} = \frac{C_n \sin((A_{n0}-\omega_{Dn})t) - (A_{n0}-\omega_{Dn})\cos((A_{n0}-\omega_{Dn})t)}{C_n^2 + (A_{n0}-\omega_{Dn})^2} \tag{B.3}$$

$$A_{n3} = \frac{C_n \cos((A_{n0}+\omega_{Dn})t) + (A_{n0}+\omega_{Dn})\sin((A_{n0}+\omega_{Dn})t)}{C_n^2 + (A_{n0}+\omega_{Dn})^2} \tag{B.4}$$

$$A_{n4} = \frac{C_n \cos((A_{n0}-\omega_{Dn})t) + (A_{n0}-\omega_{Dn})\sin((A_{n0}-\omega_{Dn})t)}{C_n^2 + (A_{n0}-\omega_{Dn})^2} \tag{B.5}$$

$$A_{n5} = \omega_{Dn}\left(A_{n0}^2 + C_n^2 + \omega_{Dn}^2\right)\sin(\omega_{Dn}t) - C_n\left(A_{n0}^2 - C_n^2 - \omega_{Dn}^2\right)\cos(\omega_{Dn}t) \tag{B.6}$$

$$A_{n6} = A_{n0}\left(\left(A_{n0}^2 - C_n^2 + \omega_{Dn}^2\right)\cos(\omega_{Dn}t) - 2C_n\omega_{Dn}\sin(\omega_{Dn}t)\right) \tag{B.7}$$

$$A_{n7} = \omega_{Dn}\left(A_{n0}^2 + C_n^2 + \omega_{Dn}^2\right)\cos(\omega_{Dn}t) + C_n\left(A_{n0}^2 - C_n^2 - \omega_{Dn}^2\right)\sin(\omega_{Dn}t) \tag{B.8}$$

$$A_{n8} = A_{n0}\left(\left(A_{n0}^2 - C_n^2 + \omega_{Dn}^2\right)\sin(\omega_{Dn}t) + 2C_n\omega_{Dn}\cos(\omega_{Dn}t)\right) \tag{B.9}$$

$$D_n = \left(A_{n0}^2 + C_n^2 + \omega_{Dn}^2\right)^2 - \left(2A_{n0}C_n\right)^2 \tag{B.10}$$

$$E_n = \exp(\zeta_n\omega_n t) \tag{B.11}$$

$$I_{n1} = \int \sin\left(\frac{\lambda_n V t}{L}\right)\cos(\omega_{Dn}t)\exp(\zeta_n\omega_n t)\, dt = \frac{E_n}{2}\left(A_{n1} + A_{n2}\right) \tag{B.12}$$

$$I_{n2} = \int \cos\left(\frac{\lambda_n V t}{L}\right)\cos(\omega_{Dn}t)\exp(\zeta_n\omega_n t)\,dt = \frac{E_n}{2}\left(A_{n3} + A_{n4}\right) \tag{B.13}$$

$$I_{n3} = \int \sinh\left(\frac{\lambda_n V t}{L}\right)\cos(\omega_{Dn}t)\exp(\zeta_n\omega_n t)\,dt = \frac{E_n}{D_n}\left(A_{n5}\sinh(\lambda_n t) + A_{n6}\cosh(\lambda_n t)\right) \tag{B.14}$$

$$I_{n4} = \int \cosh\left(\frac{\lambda_n V t}{L}\right)\cos(\omega_{Dn}t)\exp(\zeta_n\omega_n t)\,dt = \frac{E_n}{D_n}\left(A_{n5}\cosh(\lambda_n t) + A_{n6}\sinh(\lambda_n t)\right) \tag{B.15}$$

$$J_{n1} = \int \sin\left(\frac{\lambda_n V t}{L}\right)\sin(\omega_{Dn}t)\exp(\zeta_n\omega_n t)\,dt = \frac{E_n}{2}\left(-A_{n3} + A_{n4}\right) \tag{B.16}$$

$$J_{n2} = \int \cos\left(\frac{\lambda_n V t}{L}\right)\sin(\omega_{Dn}t)\exp(\zeta_n\omega_n t)\,dt = \frac{E_n}{2}\left(A_{n1} - A_{n2}\right) \tag{B.17}$$

$$J_{n3} = \int \sinh\left(\frac{\lambda_n V t}{L}\right)\sin(\omega_{Dn}t)\exp(\zeta_n\omega_n t)\,dt = \frac{E_n}{D_n}\left(-A_{n7}\sinh(\lambda_n t) + A_{n8}\cosh(\lambda_n t)\right) \tag{B.18}$$

$$J_{n4} = \int \cosh\left(\frac{\lambda_n V t}{L}\right)\sin(\omega_{Dn}t)\exp(\zeta_n\omega_n t)\,dt = \frac{E_n}{D_n}\left(-A_{n7}\cosh(\lambda_n t) + A_{n8}\sinh(\lambda_n t)\right) \tag{B.19}$$

References

[1] Eu-Rail, Europe's Rail Joint Undertaking (EU-Rail), 2022. https://rail-research.europa.eu/.
[2] Eu-Rail, 2023. InBridge4EU, https://inbridge4eu.eu/.
[3] INF TSI. Technical Specifications for Interoperability Relating to the 'Infrastructure' Subsystem of the Rail System in the European Union, Brussels, Belgium, 2019.
[4] LOC & PAS TSI. Technical Specification for Interoperability Relating to the 'Rolling Stock - Locomotives and Passenger Rolling Stock' Subsystem of the Rail System in the European Union, Brussels, Belgium, 2019.
[5] European Committee for Standardization. EN 15528. Railway Applications - Line Categories for Managing the Interface between Load Limits of Vehicles and Infrastructure, Brussels, Belgium, 2021.
[6] European Committee for Standardization. EN 1990-Annex A2. Eurocode 0: Basis of Structural Design - Annex 2: Application for Bridges (Normative), Brussels, Belgium, 2001.
[7] European Committee for Standardization. EN 1991-2 Eurocode 1: Actions on Structures - Part 2: Traffic Loads on Bridges, Brussels, Belgium, European Committee for Standardization, 2003.
[8] O.S. ko Bigus, P. Śniady, F. Zakęś, Application of Volterra integral equations in the dynamics of a multi-span Rayleigh beam subjected to a moving load, Mech. Syst. Signal Process. 121 (2019) 777–790.
[9] P. Reumers, G. Lombaert, G. Degrande, The effect of foundation-soil-foundation interaction on the response of continuous, multi-span railway bridges, Eng. Struct. 299 (2024) 117096.
[10] X. Zhang, M. Zhao, H. Liang, Improved algorithms applying the numerical Laplace method for response analyses of Timoshenko beam subjected to typical external loads, Int. J. Mech. Sci. 144 (2018) 186–204.
[11] H.A. F.A. Santos, A new finite element formulation for the dynamic analysis of beams under moving loads, Comput. Struct. 298 (2024) 107347.
[12] A.E. Martínez-Castro, P. Museros, A. Castillo-Linares, Semi-analytic solution in the time domain for non-uniform multi-span Bernoulli-Euler beams traversed by moving loads, J. Sound Vib, 294 (1) (2006) 278–297.
[13] E. García-Macías, A.E. Martínez-Castro, Hilbert transform-based semi-analytic meta-model for maximum response envelopes in dynamics of railway bridges, J. Sound Vib. 487 (2020) 115618.
[14] C. Johansson, C. Pacoste, R. Karoumi, Closed-form solution for the mode superposition analysis of the vibration in multi-span beam bridges caused by concentrated moving loads, Comput. Struct. 119 (2013) 85–94.
[15] T. Schanze, Sinc interpolation of discrete periodic signals, IEEE Trans. Signal Process. 43 (6) (1995) 1502–1503.
[16] S. Maymon, A.V. Oppenheim, Sinc interpolation of nonuniform samples, IEEE Trans. Signal Process. 59 (10) (2011) 4745–4758.
[17] S.S. Eshkevari, A.N. Pakzad, M. Takáč, T.J. Matarazzo, Modal identification of bridges using mobile sensors with sparse vibration data, J. Eng. Mech. 146 (4) (2020).
[18] L. Frýba, Vibration of Solids and Structures Under Moving Loads, 3rd ed., Thomas Telford Publishing, London, UK, 1999.
[19] E. Jarlebring, W. Michiels, K. Meerbergen, A linear eigenvalue algorithm for the nonlinear eigenvalue problem Numerische Mathematik, 122, 2012.
[20] E. Jarlebring, M. Bennedich, G. Mele, E. Ringh, P. Upadhyaya, NEP-PACK: a Julia package for nonlinear eigenproblems, 2018. https://github.com/nep-pack.
[21] R.W. Clough, J. Penzien, Dynamics of Structures. 2nd ed, McGraw-Hill, New York, USA, New York, USA, 1993.
[22] A. Hiraoka, G. Hayashi, T. Yamaguchi, Influence of intermediate hinge damage on bridge response and modal parameters of cantilever-suspended girder bridge, in: P. Rizzo, A. Milazzo (Eds.), European Workshop on Structural Health Monitoring, Cham, Springer International Publishing, 2023, pp. 745–753.
[23] European Railway Research Institute (ERRI), Design of Railway Bridges for Speed up to 350 km/h: Dynamic Loading Effects Including Resonance, European Railway Research Institute (ERRI), 1998, D214.
[24] N. Shibata, F. Petrogalli, SLEEF: A portable vectorized library of C standard mathematical functions, IEEE Trans. Parallel Distrib. Syst. 31 (6) (2020) 1316–1327.
[25] M. Frigo, S.G. Johnson, The design and implementation of FFTW3. proceedings of the IEEE, Special issue on "Program Generation, Optimization, and Platform Adaptation 93 (2005) 216–231.
[26] Structuraldynamicsodesolvers, jl: ODE Solvers for Structural Dynamics problems in Julia, 2023. https://github.com/ONSAS/StructuralDynamicsODESolvers.jl.
[27] J. Chen, J. Revels, Robust Benchmarking in Noisy Environments, 2016.
[28] S. Danisch, J. Krumbiegel, Makie.jl: flexible high-performance data visualization for Julia, J. Open Source Softw. 6 (65) (2021) 3349.